Journal of Glaciology

Article

Cite this article: Smith T, Smith MW, Chambers JR, Sailer R, Nicholson L, Mertes J, Quincey DJ, Carrivick JL, Stiperski I (2020). A scale-dependent model to represent changing aerodynamic roughness of ablating glacier ice based on repeat topographic surveys. *Journal of Glaciology* 1–15. https://doi.org/10.1017/jog.2020.56

Received: 15 May 2020
Revised: 30 June 2020
Accepted: 1 July 2020

Key words:
Energy balance modelling; glacier melt; ice roughness; structure from motion photogrammetry

Author for correspondence:
Mark W. Smith,
E-mail: m.w.smith@leeds.ac.uk

cambridge.org/jog

A scale-dependent model to represent changing aerodynamic roughness of ablating glacier ice based on repeat topographic surveys

Thomas Smith[1], Mark W. Smith[1], Joshua R. Chambers[1], Rudolf Sailer[2], Lindsey Nicholson[3], Jordan Mertes[4], Duncan J. Quincey[1], Jonathan L. Carrivick[1] and Ivana Stiperski[3]

[1]School of Geography and water@leeds, University of Leeds, Leeds, LS2 9JT, UK; [2]Department of Geography, Universität Innsbruck, Bruno Sander Haus, Innrain 52, Innsbruck, A-6020, Austria; [3]Department of Atmospheric and Cryospheric Sciences, Universität Innsbruck, Bruno Sander Haus, Innrain 52, Innsbruck, A-6020, Austria and [4]Centre for Environmental and Climate Research, Lund University, Ekologihuset, Sölvegatan 37, Lund, Sweden

Abstract

Turbulent fluxes make a substantial and growing contribution to the energy balance of ice surfaces globally, but are poorly constrained owing to challenges in estimating the aerodynamic roughness length (z_0). Here, we used structure from motion (SfM) photogrammetry and terrestrial laser scanning (TLS) surveys to make plot-scale 2-D and 3-D microtopographic estimations of z_0 and upscale these to map z_0 across an ablating mountain glacier. At plot scales, we found spatial variability in z_0 estimates of over two orders of magnitude with unpredictable z_0 trajectories, even when classified into ice surface types. TLS-derived surface roughness exhibited strong relationships with plot-scale SfM z_0 estimates. At the glacier scale, a consistent increase in z_0 of ~0.1 mm d^{-1} was observed. Space-for-time substitution based on time since surface ice was exposed by snow melt confirmed this gradual increase in z_0 over 60 d. These measurements permit us to propose a scale-dependent temporal z_0 evolution model where unpredictable variability at the plot scale gives way to more predictable changes of z_0 at the glacier scale. This model provides a critical step towards deriving spatially and temporally distributed representations of z_0 that are currently lacking in the parameterisation of distributed glacier surface energy balance models.

1. Introduction

The physical roughness of a surface exerts drag on the air moving over it, leading to instabilities that drive turbulence within a wind profile and vertical mixing of air through turbulent eddies (Cuffey and Paterson, 2010). Over ice surfaces, such turbulence can deliver energy to the glacier surface in two ways:

(1) if the air in the boundary layer directly above the ice surface is warmer than the surface itself, then sensible heat is transferred to the ice surface (Morris, 1989);
(2) if the overlying air is more humid than the ice surface, eddies drive the transfer of latent heat to the surface through condensation or deposition (Cuffey and Paterson, 2010).

Accordingly, sensible and latent heat transfer are referred to as turbulent fluxes; both can be net sinks or sources of heat energy to ice surfaces under differing climatic conditions (Lewis and others, 1998; Greuell and others, 2001; Sicart and others, 2005). Figure 1 compares the balance of the turbulent and radiative components of the surface energy balance (SEB) for a global compilation of 47 glaciers during their ablation seasons. Typically, the literature gives more attention to the calculation of radiative fluxes, which have a much greater role in supplying melt energy to ice surfaces globally than turbulent fluxes. While not the dominant source of melt energy, turbulent fluxes can have a substantial contribution to a glacier SEB, particularly: (i) at high latitudes in the northern hemisphere where ice surfaces at lower altitudes are exposed to high summer air temperatures; and (ii) in maritime conditions where windy and cloudy conditions reduce the role of short-wave and long-wave radiation, e.g. Scandinavia and the West coast of New Zealand (Ishikawa and others, 1992; Giesen and others, 2014; Conway and Cullen, 2016). Conversely, in areas where both summer and winter temperatures remain extremely low, turbulent fluxes tend to be either very small or act as a net sink of melt energy (Sicart and others, 2005, Bravo and others, 2017).

Figure 1 demonstrates that turbulent fluxes can contribute >20% of total energy available for melt over an ablation season. However, for shorter timescales they can contribute as much as 76% to the SEB of an ice surface (e.g. Fausto and others, 2016*a*). Moreover, there is growing recognition that the role of turbulent fluxes in driving glacier ice melt is increasing as global climate moves towards wetter, windier and warmer conditions (van den Broeke and others, 2008; van den Broeke and others, 2011; Franco and others, 2013). This is particularly the case in polar regions where climate warming is amplified (IPCC, 2013).

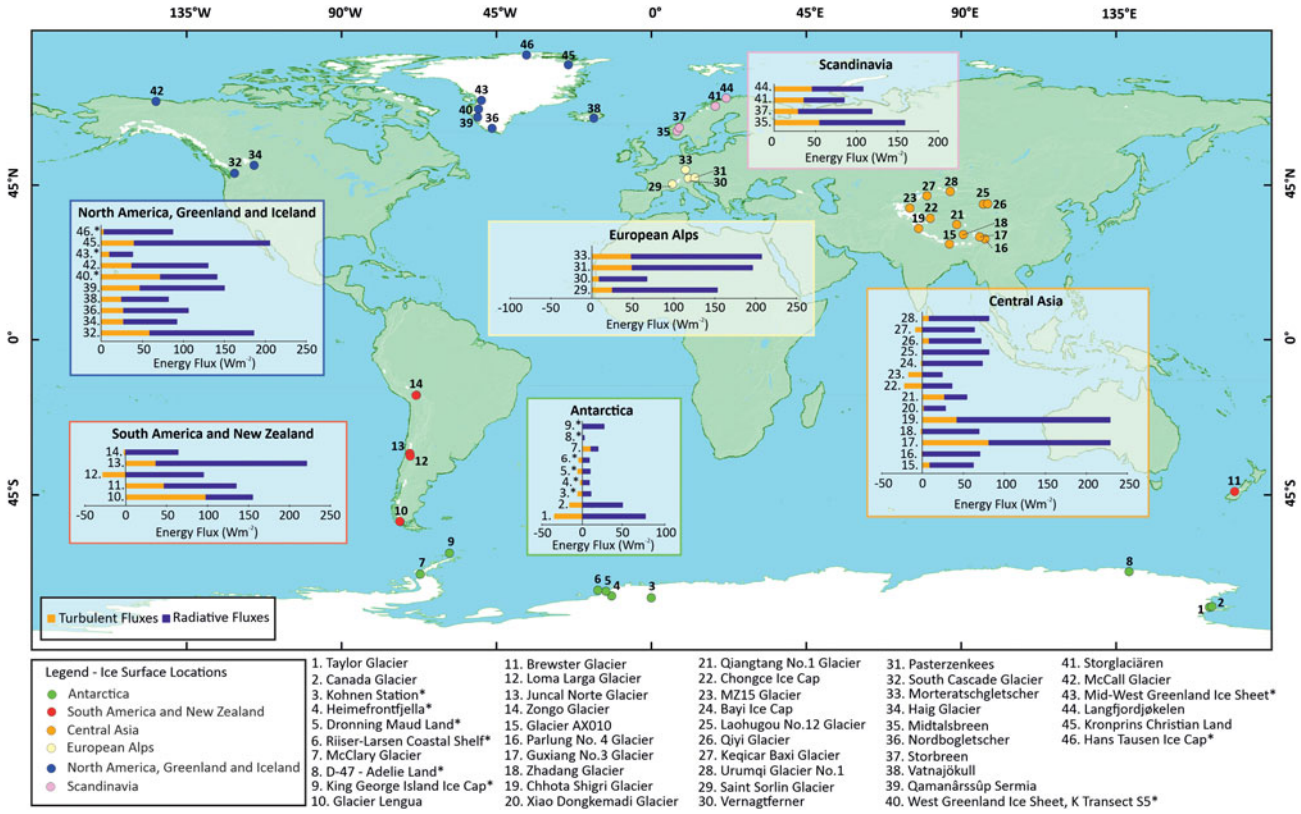

Fig. 1. The role of radiative and turbulent fluxes globally for studies on permanent snow or ice surfaces during the ablation season and of duration longer than 2 weeks. References for each of these data points are provided in online Supplementary Table S1. Values over ice sheets are indicated with an asterisk

A potential major source of error within turbulent flux calculations is the estimation of the aerodynamic roughness length (z_0), defined as the height above an ice surface at which the wind velocity drops to zero (Smith, 2014). Estimation of z_0 is challenging and often requires extensive and intensive field datasets. Three methods are commonly applied in order to assess the value for z_0 of a surface: (i) direct observations of turbulence using sonic anemometers (e.g. Greuell and Genthon, 2004; Fitzpatrick and others, 2019); (ii) extrapolation from log-linear profiles of horizontal wind speed and air temperature (e.g. Ishikawa and others, 1992; Bintanja and van den Broeke, 1995; Hock and Holmgren, 2005); and (iii) estimation using surface microtopographic data, usually following approaches based on Lettau (1969).

Both sonic anemometers and wind profiles only provide point values, and require expensive equipment deployed over long periods during which continuous maintenance is needed (Munro, 1989; Gromke and others, 2011; Nicholson and others, 2016; Radić and others, 2017). Moreover, substantial assumptions, sensitivities and uncertainties remain inherent to both techniques (cf. Chambers and others, 2019). Yet, z_0 has been observed to vary over several orders of magnitude through both space and time (e.g. Bintanja and van den Broeke, 1995; Smeets and others, 1999; Guo and others, 2011; Sicart and others, 2014; Nicholson and others, 2016; Quincey and others, 2017; Fitzpatrick and others, 2019). This variability is problematic because turbulent flux calculations are sensitive to z_0; an order of magnitude change in z_0 has been reported to lead to a doubling in the calculated value for turbulent fluxes (Munro, 1989; Brock and others, 2000). Despite this sensitivity, it is typically assumed that z_0 is spatially uniform (e.g. Azam and others, 2014; Giesen and others, 2014; Sun and others, 2018), temporally uniform (e.g. Greuell and Smeets, 2001; Ebrahimi and Marshall, 2016; Schmidt and others, 2017), or that z_0 can be treated as a model tuning parameter, used to calibrate models (e.g. Anslow and others, 2008; Hoffman and others, 2008; Favier and others, 2011). Each of these assumptions introduces considerable uncertainty into turbulent flux estimations and could conceal model deficiencies.

While temporal variability in z_0 is well documented both over an entire ablation season and over shorter timescales, there is disagreement on the extent to which this variation is progressive. Evidence exists for several possibilities: (i) multiple contrasting temporal trends over a single glacier (Brock and others, 2006; Smith and others, 2016); (ii) no discernible trends in z_0 (Sicart and others, 2014; Fitzpatrick and others, 2019); (iii) progressive increase of z_0 (Smeets and van den Broeke, 2008; Nicholson and others, 2016) and (iv) a clear evolution of z_0 during the melt season, with initially low z_0 increasing as snow cover melts to expose underlying ice, followed by a decrease in z_0 as bare ice is exposed and a second period of increasing z_0 as melt causes the development and growth of meltwater channels and ice hummocks leading to $z_0 > 10$ mm (Guo and others, 2011).

Given the pronounced spatial and temporal variability in z_0, its impact on turbulent flux estimates and the potential increase in importance of turbulent fluxes for melt with changing climate, there is a clear need to better understand the spatial and temporal variability of z_0. Such work is timely as distributed melt models are increasingly able to implement distributed and potentially dynamic estimates of z_0. While z_0 calculation from sonic anemometers or wind profiles is too data intensive to adequately sample this variability, the recent proliferation in the availability of high-resolution topographic data using structure for motion (SfM) photogrammetry (e.g. Irvine-Fynn and others, 2014; Smith and others, 2016; Miles and others, 2017; Quincey and others, 2017) and via both terrestrial and aerial light detection and ranging (LiDAR) techniques (e.g. Smith and others, 2016; Fitzpatrick and others, 2019) makes the microtopographic approach the best means of accounting for the spatial and temporal variability of z_0. Recently, 3-D methods of estimating z_0 from topographic data (e.g. Smith and others, 2016) have

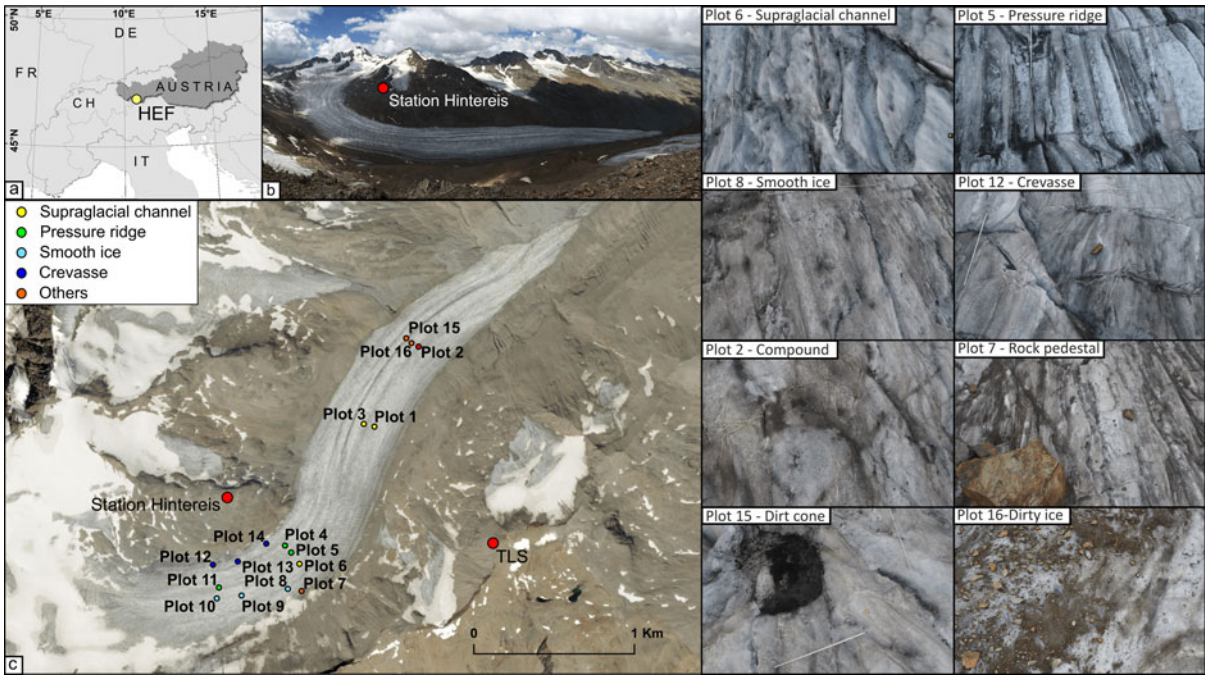

Fig. 2. (a) Location of Hintereisferner (HEF) within Austria; (b) Hintereisferner viewed from the southeast, close to the Terrestrial Laser Sanner location (3 August 2018). (c) Plot locations and contemporary glacier extent (3 August 2015); photos – example imagery for each ice facies of dimensions ~6 m × 5 m. Source for imagery in (c): Esri, Orthofoto Tirol.

sought to improve upon the more conventional 2-D profile-based methods and make use of the available topographic data. Initial attempts to upscale plot-based microtopographic estimates of z_0 to the glacier scale are promising (e.g. Smith and others, 2016), and the use of topographic data acquired from terrestrial and aerial LiDAR and potentially also from satellite imagery could allow spatially distributed representations of z_0 to become incorporated into distributed snow and ice melt models. Certainly, high-resolution stereo imagery from satellites such as WorldView and Pléiades has recently shown great promise in mapping snow depth (e.g. Marti and others, 2016; Deschamps-Berger and others, 2020; Shaw and others, 2020) and estimating glacier mass balance (e.g. Belart and others, 2017; Shean and others, 2020) and, although challenging, may also be suitable to observe z_0 variability.

Therefore, the aims of this study were: (i) to quantify at different scales the spatial and temporal variability of z_0 over glacier ice during peak melt season and (ii) to develop a theoretical representation of z_0 evolution that can be used as a foundation for more robust inclusion of z_0 dynamics in distributed SEB models.

2. Methods and study site

2.1 Study site

Hintereisferner (46°48′N, 10°47′E) is a ~6 km long valley glacier (Fig. 2), located in the catchment of Rofenache in the southern Ötztal Alps, Austria (Strasser and others, 2018). The glacier ranges from 3739 m a.s.l. at its highest point (Weißkugel) to 2498 m a.s.l. at the glacier terminus. The glacier has been studied extensively through ablation stake measurements (e.g. Blümcke and Hess, 1899; Ambach, 1961; van de Wal and others, 1992; Kuhn and others, 1999), observation of accumulation in snow pits (e.g. Patzelt, 1970; Kuhn and others, 1999) dye tracing of the internal drainage system (e.g. Behrens and others, 1975), SEB observations (e.g. van de Wal and others, 1992), numerical modelling of flow and mass balance (e.g. Greuell and others, 1992; Escher-Vetter and others, 2009; Fischer, 2010), digital elevation model (DEM) analysis (e.g. Geist and Stotter, 2007), LANDSAT imagery reflectance analysis (e.g. Koelemeijer and others, 1993) and airborne photogrammetry (e.g. Patzelt, 1980; Lambrecht and Kuhn, 2007). Supplementing much of this research is one of the longest continuous records of mass balance in the world (1952/53–present; Fischer, 2010), and extensive observations of glacier length which have been made since 1847 (Greuell, 1992).

As of 2018, the glacial extent of Hintereisferner was 6.22 km^2; this value represents a large reduction from the extent during the Little Ice Age (LIA) in 1855. The glacier has been in almost constant retreat since the LIA (Greuell, 1992); the rate of decline is currently rapid – from 2001 to 2011 alone the glacier terminus retreated 390 m (Klug and others, 2018). The ice is also thinning; between 1953 and 2006, surface lowering of over 100 m was observed in the vicinity of the glacier terminus, while up-glacier the surface elevation decreases were <40 m (Fischer, 2010). Such geometry changes and rapid mass loss is characteristic of glaciers throughout Austria (Fischer and others, 2015; Carrivick and others, 2015*a*) and across the entire European Alps with many glaciers now shrinking at a rate of 1% of their area per annum (Vincent and others, 2017).

Our field campaign lasted 15 d between 1 and 15 August 2018 and primarily involved the repeat survey of 16 plots of 10 m × 10 m. A wind tower comprising five NRG 40 cup anemometers, one NRG 200P wind vane and five shielded and passively-ventilated Extech RHT10 temperature and humidity loggers was installed at Plot 2 for the duration of the study. Temperature (5 min average) and wind speed and direction (30 min average) data are displayed in Figure 3. Day time temperatures (Fig. 3a) over the glacier reached peaks of >10°C for all study days, the highest temperature recorded was 19.8°C occurring in the afternoon of the 5th day of study. Minimum diurnal temperatures were always <5°C but did not drop below 2°C. Mean wind speed (Fig. 3b) was 2.5 m s^{-1} with peak values exceeding 5 m s^{-1}. Mean wind direction was 165° relative to the down-glacier direction, demonstrating that katabatic winds dominate over Hintereisferner during the ablation season in accordance with previous studies (Obleitner, 1994). Precipitation throughout the field campaign was mainly constrained to convective thunderstorms occurring in the afternoon; particularly heavy events were noted on 1st, 6th, 10th and 13th days of study.

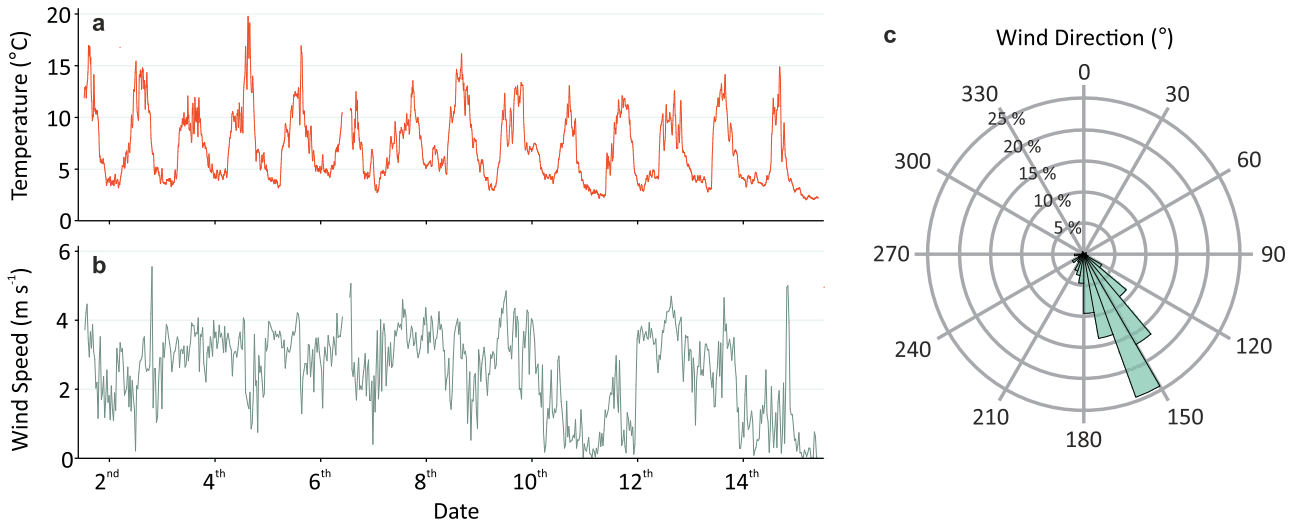

Fig. 3. (a) Temperature (°C) and (b) wind speed at ~1 m ($m\,s^{-1}$) throughout the study period (1–15 August 2018). A small gap within the data exists due to a fault with the data logger during the 6th day of study. (c) Wind direction (% of time) with down-glacier direction set to 0°.

2.2 Plot surveys

Sixteen plots containing eight distinct ice facies distributed around the ablation area of the glacier were identified (Fig. 2). Plots of 10 m × 10 m with a spatial resolution of <10 mm are adequate for characterisation of aerodynamic roughness (Rees and Arnold, 2006). Following an initial glacier survey, the most common ice facies were identified as: Supraglacial Channels, Pressure Ridges, Smooth Ice and Crevasses. Three replicate plots were demarcated for each of these surface roughness types to test for consistency in response. In addition, one plot was sampled for each of the less prominent ice facies identified: Rock Pedestal, Dirt Cone, Dirty Ice and Compound (i.e. multiple co-located features). Over 15 d, starting on 1 August 2018, each plot was surveyed with an average interval of 4 d; however, owing to inclement weather and logistical difficulties, this interval varied between plots (3–5 d).

High-resolution topographic data for the 16 plots were obtained via standard SfM photogrammetry workflows (James and others, 2017; O'Connor and others, 2017). A survey pole extended to a vertical height of ~6 m allowed for a large image footprint, a high degree of image overlap and good coverage of the plot area with a relatively low number of images. Approximately five rows of 12 off-nadir photographs with intervals of ~1.5 m between successive rows were taken during each survey to achieve a target of 80% sidelap and 60% frontlap between images. On each row, images were taken from different directions with additional images taken from the plot edges. Details of the camera parameters are displayed in Table 1.

Each plot was marked out using five ground control points (GCPs) placed on areas of flat ice in the corners and centre, secured into the ice with a metal peg and surveyed using a Leica GS10 differential GPS system in real-time kinematic (RTK) mode. Mean GCP accuracy was sub-centimetre for each plot. Owing to down-glacier movement of the ice patch and the dynamic nature of the glacier surface, GCP locations were resurveyed at each visit. The same ice surface was resurveyed each time, thus the absolute coordinates of the plots translated down-glacier through the survey period. SfM photogrammetry was performed using Agisoft Photoscan Professional Edition Version 1.4.0 following the workflow of James and others (2017). Typically, total 3-D root mean square (RMS) GCP error was ~0.02 m and RMS re-projection error generally <2 pixels. Dense point clouds were cropped to 10 m × 10 m centred on the middle GCP and octree subsampled to a point density $\sim 4 \times 10^4$ points m^{-2} ($\sim 4 \times 10^6$ points per plot). The subsampled point clouds were then rasterised to create a DEM of resolution 5×10^{-3} m for all 59 surveys, using the mean elevation within each cell.

Table 1. Key features of SfM photogrammetry surveys and camera parameters

Specifications	Primary camera	Secondary camera
Make and model	Olympus EM 10	Canon PowerShot SX600 HS
Lens model	M. Zuiko Digital 14–42 mm	Built in
Weight (g)	396	188
Resolution (MP)	16.1	16.0
Sensor size (mm)	17.3 × 13.0	6.2 × 4.6
Image size (pixels)	4608 × 3456	4608 × 3456
Pixel pitch (μm)	3.74	1.34
GSD (mm)[a]	0.80	0.32
Focal length	~28 mm	~25 mm
Maximum (mean) images per plot	71 (64)	
Survey platform	Survey Pole at ~ 6 m above the ice surface	
Camera locations	360° survey	
Angle of imagery	~20° off vertical	
Camera trigger	Remote (via Smartphone)	

[a]Calculated ground surface distance (GSD) is based on the assumption that photographs were taken nadir to the surface. The secondary camera was used for six surveys due to technical issues with the primary camera.

2.3 Topographic z_0 estimation

From empirical work, Kutzbach (1961) and Lettau (1969) proposed a relationship to relate the surface form and density of roughness elements to z_0:

$$z_0 = 0.5h^* \frac{s}{S_A} \quad (1)$$

where 0.5 is the average drag coefficient of one roughness element, h^* is the average peak vertical extent of roughness elements (mm), s is the silhouette area of the average obstacle (mm^2) and S_A is the specific horizontal area of the plot (mm^2), given by

$$S_A = \frac{A}{n} \quad (2)$$

where n is the number of obstacles and A is the total area of site (mm^2).

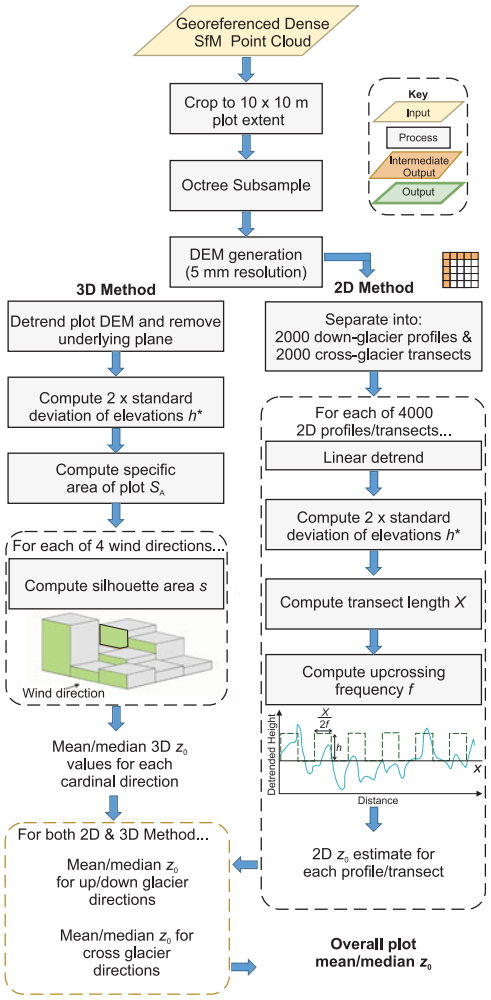

Fig. 4. Methodological steps for z_0 calculation.

In this study, we derived two alternative z_0 estimates from SfM-derived topographic data: first, the 2-D transect method of Munro (1989), and secondly, a more recently developed 3-D method that estimates z_0 from DEMs. While the 3-D method makes better use of the available topographic data and permits several assumptions to be relaxed, we also present results using the more conventional 2-D method to facilitate comparison between this and previous studies. The steps required to calculate z_0 using both methods are summarised in Figure 4.

Munro (1989) adapted Eqn (1) to allow for estimates of z_0 from transects. The method of Munro (1989) assumes that irregularly distributed roughness elements deviating around a mean elevation can be simplified to regularly distributed rectangles of height equal to h^* thereby removing the need to make an assessment of surface form in the calculation of silhouette area (s). Silhouette area is simply given by:

$$s = \frac{2\sigma_d X}{2f} \tag{3}$$

where h^* is approximated to be twice the SDs of detrended elevations ($2\sigma_d$) (mm) and equal to the representative obstacle height, X is the length of the transect measured (mm) and f is the number of extensions of the transect above zero on the mean detrended plane. The specific area (S_A) can be given by:

$$S_A = \left(\frac{X}{f}\right)^2 \tag{4}$$

so that,

$$z_0 = \frac{f}{X}(\sigma_d)^2. \tag{5}$$

To allow for 2-D estimations of z_0, as per Irvine-Fynn and others (2014) and Miles and others (2017), the DEMs were divided into transects at 0.005 m intervals giving 4000 transects for each survey, with 2000 aligned across- and 2000 down-glacier. Each transect was then detrended and an estimation of z_0 was made. Transect z_0 estimates were aggregated to mean and median flow-parallel and flow-perpendicular values and directionally averaged mean and median values were also calculated.

3-D estimations of z_0 were based on the method of Smith and others (2016), which aims to relax a number of the assumptions of Munro (1989) by using detrended DEMs derived from point clouds. Silhouette area was obtained directly for each cardinal direction by summing the exposed surface areas of each cell within a raster, and the specific area was taken to be equal to the area of the plot surveyed. Following Chambers and others (2019), the height scale h^* was set to equal twice the detrended standard deviation of elevations. Directional and plot averages can then be extracted for z_0 estimation.

Herein, the direction of transect z_0 estimates within each plot refers to the wind direction rather than the transect orientation, i.e. transects aligned across the glacier are referred to as 'parallel' (as roughness elements are exposed to a glacier flow-parallel wind) and transects aligned down-glacier are referred to as 'perpendicular' (as roughness elements are exposed to a glacier flow-perpendicular wind). For 3-D estimates up/down averaged values are exposed to a katabatic or anabatic flow and across values are exposed to an across glacier wind.

2.4 Glacier-scale surveys

Separate surveys of the upper and lower glacier were taken using a RIEGL VZ-6000 Terrestrial Laser Scanner on 3, 7, 12 and 16 August 2018. Combined, these surveys cover a glacier area of ~2 km^2. The TLS was located close to the summit of Im Hinteren Eis allowing almost the entire ablation zone to be encompassed within its field of view (Fig. 2). The near infrared laser wavelength of the RIEGL VZ-6000 is well suited to measurements of snow and ice surfaces and can achieve data acquisition rates of up to 220 000 measurements per second over a range of >6000 m within a 60° and 360° field of view vertically and horizontally, respectively (RIEGL, 2019). Due to high surface reflectivity and periods of low visibility, the laser pulse repetition rate was set to 30 kHz, extending the range of measurements, but reducing data acquisition rate to ~23 000 measurements per second. An angular increment of 0.01° allowed for horizontal and vertical spatial resolution of ~0.17 m at a range of 1000 m giving theoretical point densities of 10 points m^{-2} for the centre of the glacier and 2 points m^2 on the accumulation zone. Manufacturer stated accuracy and precision are 0.015 and 0.010 m, respectively (RIEGL, 2019) and initial analysis suggests only a 0.15 m deviation in elevations between TLS and airborne laser scanning of Hintereisferner and deviations <0.10 m between TLS scans. The largest source of associated error is likely to be caused by beam divergence (Carrivick and others, 2015*b*), which is stated as 0.12 m at a range of 1000 m.

TLS data were processed using the open-source topographic point cloud analysis toolkit (Brasington and others, 2012). Data were segregated into a regular grid of cell size 10 m × 10 m. A triangular tessellation between adjoining cells was then used to reconstruct the local surface and detrend the points relative to these planes. Elevation statistics were then calculated on a

cell-by-cell basis. Following Smith and others (2016), the standard deviation of the detrended elevations was used to represent TLS roughness (TLS σ_d).

To test for an underlying progressive evolution of z_0, a space-for-time substitution was used to artificially extend the observation period to 65 d. Two Canon EOS1200D single-lens reflex time-lapse cameras (https://www.foto-webcam.eu/webcam/hintereisferner1/2018/08/01/1200) mounted on the TLS cabin enabled the snow line to be tracked from the start of the 2018 ablation season until the study period. The snowline was digitised on each available image and converted into polygons classifying glacier ice areas into zones of exposure length. The glacier was classified into sections which have been exposed to melt for a given period of time. z_0 was estimated within each section and the effect of exposure time on z_0 observed.

2.5 Upscaling

To upscale plot-based SfM derived z_0 estimates to the glacier scale, a relationship between TLS σ_d and z_0 was established. TLS data were cropped to the extent of each SfM plot survey that took place within ± 1 d of a TLS scan ($n = 49$). One plot from each of the major ice facies was withheld for validation prior to regression analysis. Owing to concerns over the reproducibility of Crevasse and Rock Pedestal plots, these were excluded from the regression analysis. Linear regression relationships were formed between the remaining 24 TLS σ_d values and SfM z_0 estimates. These regression relationships were then applied to the glacier-scale TLS surveys for distributed z_0 estimates.

2-D and 3-D SfM z_0 estimates were made for each plot in multiple directions. To inform the linear regression relationships, the value most representative of z_0 during prevailing wind conditions was chosen. For the 2-D linear regression relationship plot average values of z_0 were used, which broadly give correct estimates of z_0 (e.g. Irvine-Fynn and others, 2014; Smith and others, 2016). The 3-D linear regression relationship was derived from down-glacier z_0 estimates that encompass the sheltering effects and topographic variability relevant to the estimation of z_0 for the prevailing wind direction. Wind direction has been identified as a likely source of error in turbulent flux calculation (Brock and others, 2006). The use of 3-D estimates which are representative of z_0 for the prevailing wind direction should reduce this error considerably.

3. Results

3.1 Spatial variability in plot-scale z_0

A statistically significant relationship between 2-D and 3-D z_0 estimates averaged for all directions was present for all surveys combined (Spearman's rank $\rho = 0.838$, $p < 0.01$, $n = 59$). The 2-D and 3-D z_0 values agree well for all surfaces where $z_0 < 5$ mm, but as z_0 increases beyond this value there is considerable deviation from a 1 : 1 fit (online Supplementary Fig. S1).

The variability of z_0 between plot types is presented in Table 2 and Figures 5 and 6. Estimates of z_0 ranged over two orders of magnitude between the eight surface types for both methods. Crevasse plots exhibited z_0 values an order of magnitude larger than other plot types for both estimation methods and wind directions, followed by Rock Pedestals and Dirt Cones. Conversely, Dirty Ice, Smooth Ice and Compound plots consistently presented the smallest z_0 values. Supraglacial Channels and Pressure Ridges both presented intermediate values of z_0 which exhibited pronounced anisotropy. However, the two calculation methods showed conflicting results on the impact of wind direction; the 2-D method showed higher z_0 values for down-glacier winds, whereas the 3-D method showed higher z_0 values for cross-glacier winds. This directional difference was apparent for all surface types.

ANOVA and Kruskal–Wallis tests were used to assess whether differences between the average values over ice facies are statistically significant. The z_0 values exhibited by Crevasse plots are distinct from the other ice facies (Fisher test $p < 0.001$). While Smooth Ice plots are characterised by lower values of z_0, this difference was only statistically significant when using the 3-D cross-wind estimates (Fisher test $p < 0.05$). z_0 estimates for Supraglacial Channel plots and Pressure Ridge plots were not distinct (Fig. 5).

3.2 Temporal variability in plot-scale z_0

The z_0 values for the repeat surveys of each plot are displayed in Figure 6. Typically, the evolution of 2-D and 3-D z_0 estimates followed the same trajectory. The z_0 values for all surface types at Hintereisferner were highly dynamic; yet, no clear trend was present over the observation period. Furthermore, no consistent response by surface type was observed.

The Supraglacial Channel plots (1, 3 and 6) displayed two distinctive trajectories: plot 1 exhibited a pronounced increase in z_0 which became more rapid between days 10 and 13, whereas plot 3 and plot 6 z_0 steadily decreased over the same period. Likewise, no consistent trajectory of z_0 was observed for the Pressure Ridge plots (4, 5 and 11): plot 4 demonstrated the highest temporal variability, with an initially rapid increase between days 2 and 4 followed by a sharp decline until day 11, and plots 5 and 11 showed only modest changes throughout the study period. Considering the Smooth Ice plots (8, 9 and 10), plot 8 displayed a gentle decline in z_0 across the observation period, whereas at plot 9 z_0 initially increased then decreased to a value similar to the starting value, and finally plot 10 provided a different evolution again, with z_0 increasing very gradually over the survey period, though changes at this plot were very small.

Table 2. Mean z_0 estimates by plot type, wind direction and estimation method

	2-D z_0 (mm)			3-D z_0 (mm)		
	Plot average	Down-glacier wind direction	Cross-glacier wind direction	Plot average	Down-glacier wind direction	Cross-glacier wind direction
Crevasse	37.05 [10.6]	35.28 [8.63]	38.83 [22.90]	24.25 [9.25]	22.85 [8.94]	25.64 [8.86]
Rock Pedestal	4.28 [0.97]	5.66 [1.14]	2.89 [0.85]	11.87 [3.01]	10.51 [3.18]	13.23 [2.85]
Supraglacial channel	5.63 [0.96]	8.10 [1.22]	3.16 [0.81]	6.27 [1.53]	5.41 [0.69]	7.13 [0.94]
Dirt Cone	5.43 [0.89]	6.38 [0.87]	4.48 [1.04]	8.48 [1.98]	7.44 [2.13]	9.52 [1.83]
Pressure Ridge	4.68 [0.87]	7.22 [1.41]	2.15 [0.34]	5.95 [1.31]	4.50 [1.55]	7.40 [1.53]
Dirty Ice	3.04 [0.66]	4.21 [0.85]	1.87 [0.46]	5.22 [1.45]	4.98 [1.39]	5.46 [1.51]
Smooth Ice	3.35 [0.66]	4.50 [0.93]	2.20 [0.71]	3.23 [0.74]	2.74 [0.69]	3.72 [0.94]
Compound	1.90	2.77	1.04	2.16	1.78	2.54

Individual plot measurements are displayed in Figure 6. The standard deviation of values is provided in square brackets.

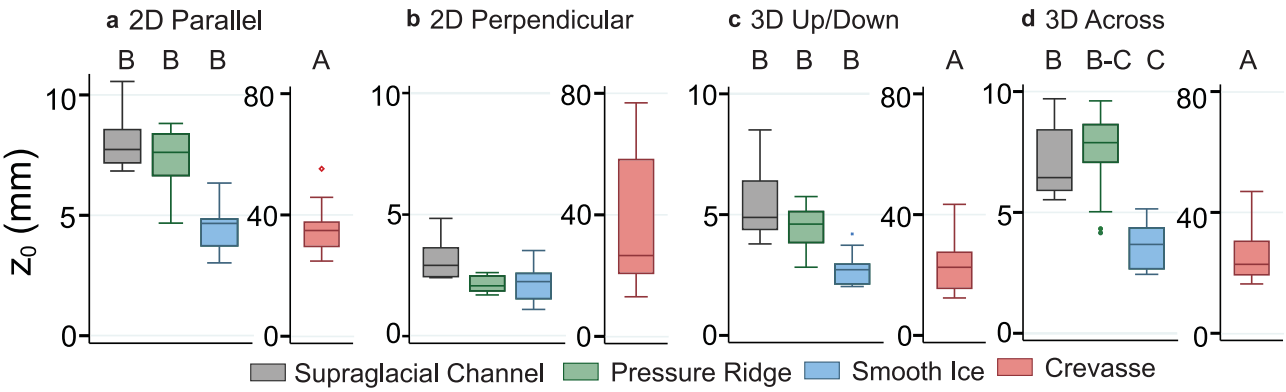

Fig. 5. A summary of the distribution of each z_0 metric for each surface type. Groupings from Fisher pairwise comparisons are displayed above the boxes. Ranges of values are indicated by the whiskers, interquartile range is indicated by the box, with the horizontal line within the box displaying the median. Points beyond 1.5 times the interquartile range from the upper/lower quartile are plotted separately.

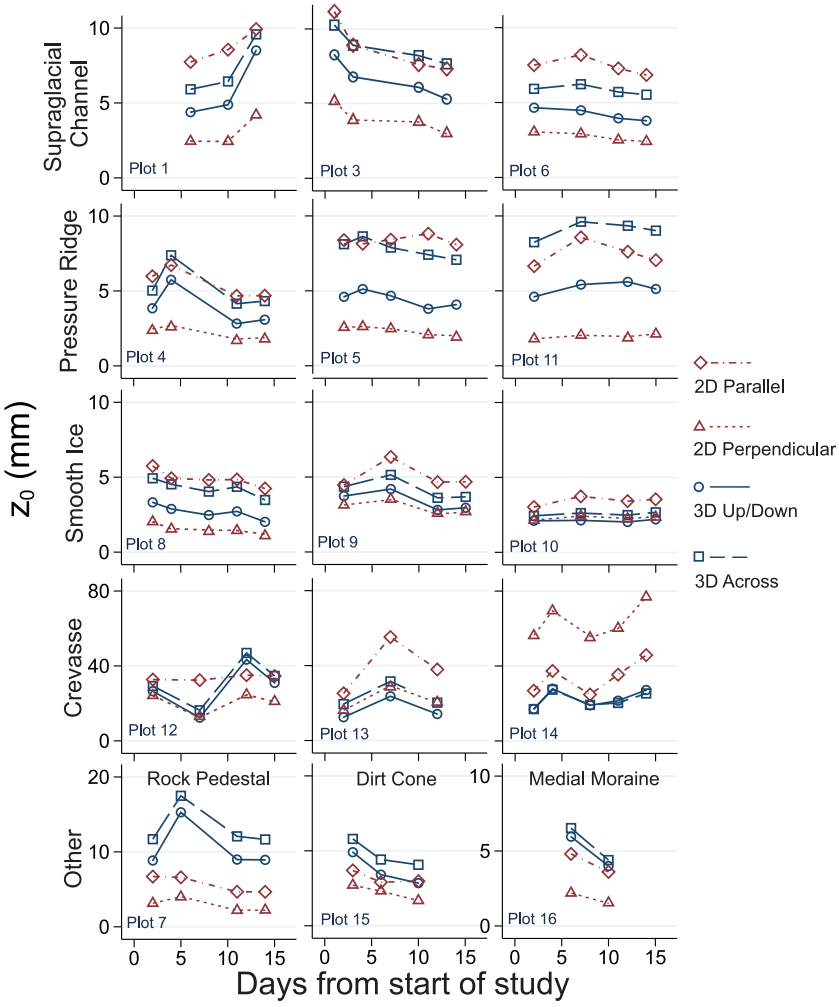

Fig. 6. Temporal change of z_0 for plots with multiple surveys. Each row displays a different surface type. Axes scales are variable to allow for a clearer display of temporal trends for Crevasse and Other sites.

The observed changes in z_0 estimates for Crevasse plots (12, 13 and 14) were more extreme with changes occurring at rates of >5.0 mm d^{-1}. These results are most likely to reflect difficulties in consistently data modelling the complex terrain present at Crevasse plots. Both the Dirt Cone (15) and Dirty Ice (16) plots showed a clear decrease in z_0 over the field campaign indicating a surface smoothing. The Rock Pedestal plot (7) displayed two different trends: the 2-D z_0 exhibited a gentle decline through the survey period, while the 3-D z_0 value showed greater variability with an initial rapid rise in z_0 followed by a decline back to the original value.

3.3 Distributed z_0 estimates at the glacier scale

TLS survey point density for the lower and upper glacier was ~15 and 20 points m^{-2}, respectively (Fig. 7a). Ice facies exhibited similar relative values for both TLS σ_d and SfM derived z_0 estimates (cf. Fig. 5 and Fig. 7). An ANOVA test indicated a statistically significant difference between the groups, while post-hoc Fisher tests showed that Crevasse plots were statistically significantly different from all other plots ($p < 0.001$) and Smooth Ice plots were significantly different from Supraglacial Channels ($p = 0.002$). Though not statistically significant ($p = 0.051$), a difference also appears

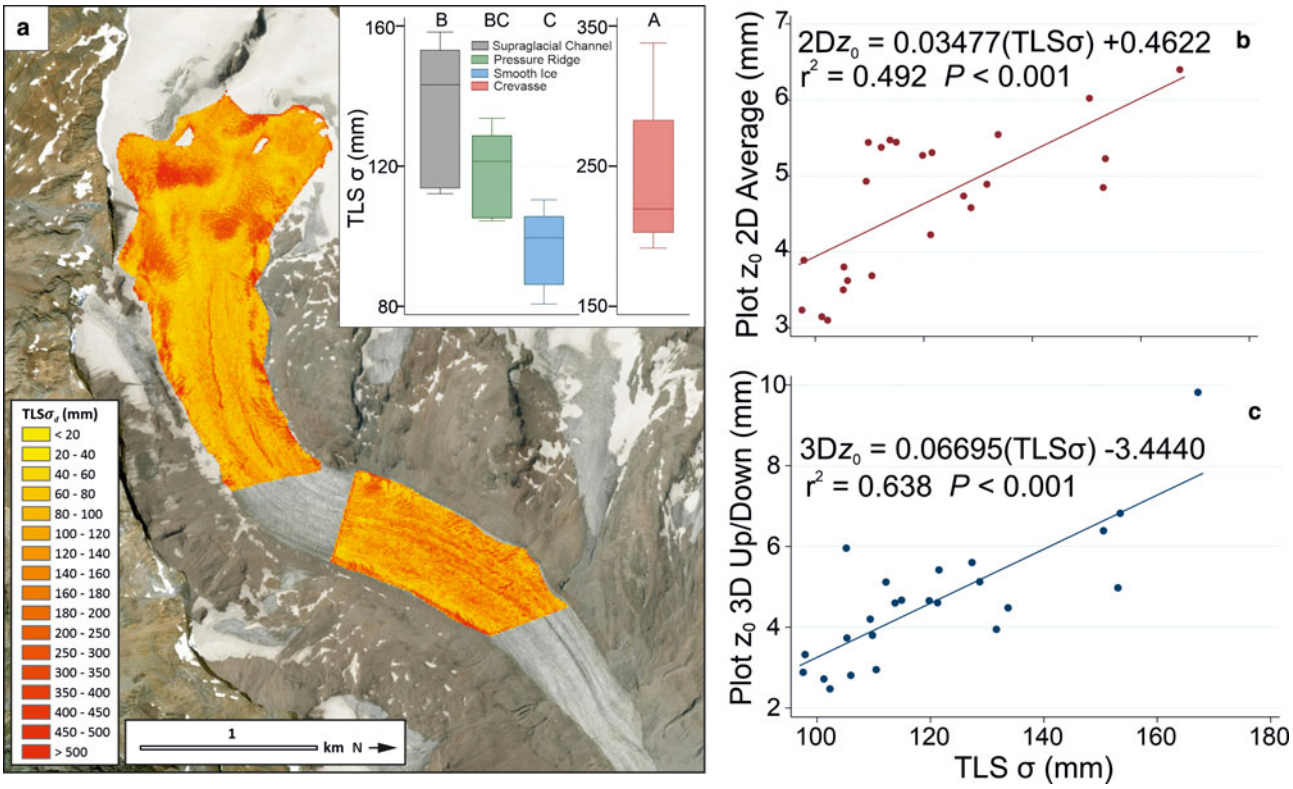

Fig. 7. (a) Glacier-wide TLS σ_d from 3 August with inset distributions for each ice surface facies (groupings from Fisher pairwise comparisons are displayed above boxes). (b) Linear regressions for 2-D and (c) 3-D estimates of z_0.

Table 3. Comparison of TLS z_0 predictions and SfM z_0 estimates for plots withheld from regression analysis

Surface type	SfM z_0 (mm)	TLS z_0 (mm)	Error (mm)
		3-D estimates	
Supraglacial Channel (Plot 1)	6.45	7.07	0.62
Pressure Ridge (Plot 4)	4.80	3.97	0.83
Smooth Ice (Plot 10)	2.12	2.59	0.47
Rock Pedestal (Plot 7)	11.03	14.46	3.43
Crevasse (Plot 14)	20.99	12.22	8.77
		2-D estimates	
Supraglacial Channel (Plot 1)	6.08	5.92	0.16
Pressure Ridge (Plot 4)	4.01	4.31	0.30
Smooth Ice (Plot 10)	2.86	3.58	0.72
Rock Pedestal (Plot 7)	4.18	9.76	5.58
Crevasse (Plot 14)	45.66	8.60	37.06

to exist between TLS σ_d values for Smooth Ice and Pressure Ridge plots.

Linear regression between TLS σ_d and both 2-D and 3-D SfM plot-scale z_0 estimates showed a reasonable fit ($r^2 = 0.49$ and 0.64, respectively) (Fig. 7c) and were used to produce glacier-scale distributed maps of z_0. Validation of the relationships using withheld data points is presented in Table 3. TLS-based estimates were particularly accurate for Supraglacial Channel, Pressure Ridge and Smooth Ice surfaces with values falling within 1 mm of SfM values. They performed less well for Rock Pedestal and Crevasse plots which were not used to inform the regression relationships.

Spatially distributed maps of TLS-estimated z_0 are displayed in Figure 8. The highest predicted values of z_0 (typically >20 mm) were located towards the margins of the glacier and in its upper reaches where the presence of crevasses led to locally high values of z_0. However, these values were most uncertain given that the regression relationships on which they are based did not perform well for these facies (Table 3). The lowest values of z_0 (0–4 mm) were located in areas of the upper glacier where snow cover was present and towards the centre of the upper glacier scan where Smooth Ice plots were surveyed. Such low values of z_0 were much less common at the lower glacier where the majority of the surface was characterised by $z_0 > 4$ mm. Maps created from both 2-D and 3-D relationships show a high level of spatial variation in z_0 over Hintereisferner; however, the use of the 3-D z_0 relationship predicted a larger range of values in z_0 arising from the higher gradient term in the linear regression relationship. For example, on the 16 August, the range in 2-D-derived z_0 estimates was 56.45 mm compared to 106.35 mm for 3-D-derived estimates.

In contrast to plot-scale trajectories, a gradual and consistent increase in TLS derived z_0 estimates was observed for both the mean glacier 2-D (0.05 mm d^{-1}) and 3-D (0.10 mm d^{-1}) estimates (Fig. 8), though glacier-scale median values exhibit a notably slower increase. Between 3 August and 16 August, z_0 estimates over Hintereisferner changed markedly in a number of areas (Fig. 8a–c). Over the crevasses at the true left margin of the glacier and in its upper reaches z_0 can be seen to increase considerably. The smooth surfaces characterised by low z_0 that surround the crevasses in the upper reaches also appeared to increase in roughness, as did the true left margin of the lower glacier. The use of a geographical coordinate system defining the TLS survey cell extents means that the down-glacier progression of surface features during the field campaign may result in local increases and decreases in roughness as features pass from cell to cell. However, the 10 m cell size means that such an effect would be limited over these time scales and this localised variability has no impact on the glacier-scale changes reported above.

The space-for-time substitution lends further support to the notion of a progressive increase in z_0 (Fig. 9). Dated snow lines, areas of the glacier surfaces classified by exposure date and histograms of TLS z_0 estimates within each section are presented in Figure 9. Ice exposed for <2 weeks had a mean and median z_0 value of less than half of ice exposed for >8 weeks. The rate of

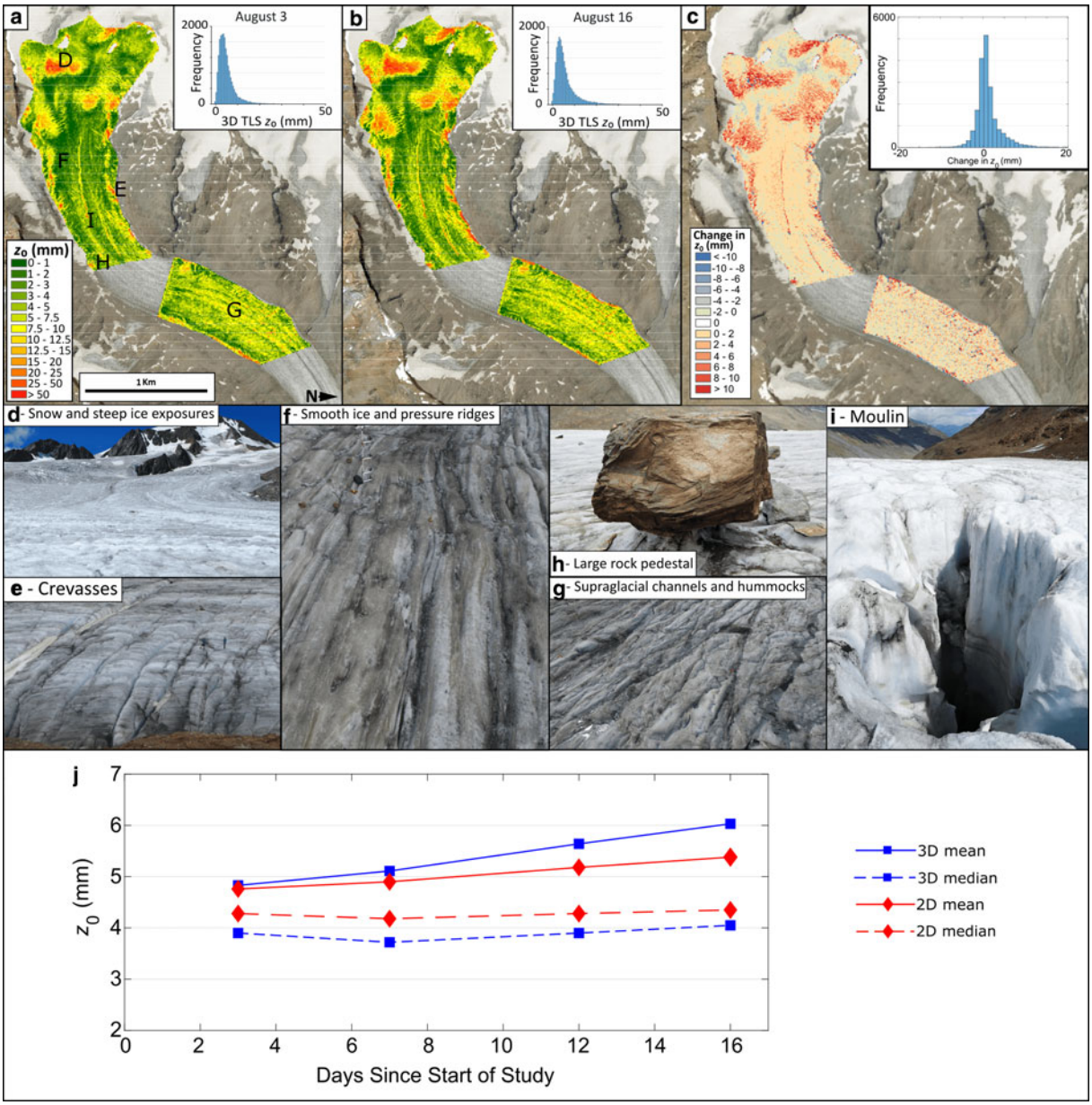

Fig. 8. Map of estimated 3-D z_0 for the 3rd (a) and 16th (b) day of study, and change in z_0 between the two dates (c). Frequency distributions for each map are inset. See online Supplementary Fig. S2 for equivalent figures for 2-D z_0. Example imagery (d–i) from the field of the different facies observed within close proximity of the areas indicated by letters in (a). Mean, median and standard deviation of glacier-scale TLS derived z_0 estimates (j).

increase was ~0.07 mm d^{-1} and appears to be relatively constant for mean values. The rate of increase in z_0 was more variable in median values, with the greatest rates of change occurring between 25 and 37 d of exposure.

Rates of change for each of the classified exposure zones were also calculated for the study period, by differencing z_0 values from the repeat TLS scans from the 3 and 16 August (Table 4). Zones which had been exposed most recently (i.e. farthest up-glacier) experienced the greatest increases in z_0 (1.46 mm). In zones that had been exposed for longer, the ice surface displayed smaller changes until >36 d (for both methods) when changes started to stabilise.

4. Discussion

4.1 Estimating z_0 from microtopographic data

The successful generation of dense point clouds for multiple surface types over Hintereisferner attests to the already recognised potential of SfM for generating microtopographic data for glacial surfaces (e.g. Irvine-Fynn and others, 2014; Chambers and others, 2019). However, the application of SfM was most challenging over Crevasse plots and over Rock Pedestal plots; gaps in the point clouds within the deep vertical crevasse walls and steep faces of rock pedestals were observed and are likely to be a consequence of imperfect image capture (given safety concerns) and unavoidable shadowing. While caution is required when interpreting microtopographically-derived z_0 values over such surfaces, this impact is limited for upscaling owing to their relatively small area at the glacier scale.

2-D and 3-D z_0 estimation methods displayed differing levels of agreement for different surface types. For surfaces devoid of large protruding roughness elements, the methods give similar results; where such roughness elements were present, there was less agreement between the two methods. Over Dirt Cone and Rock Pedestal plots 3-D z_0 estimates were typically greater than their 2-D counterparts. These findings corroborate those of Smith and others (2016) over Kårsaglaciären in northern Sweden and Quincey and others (2017) who observed that for

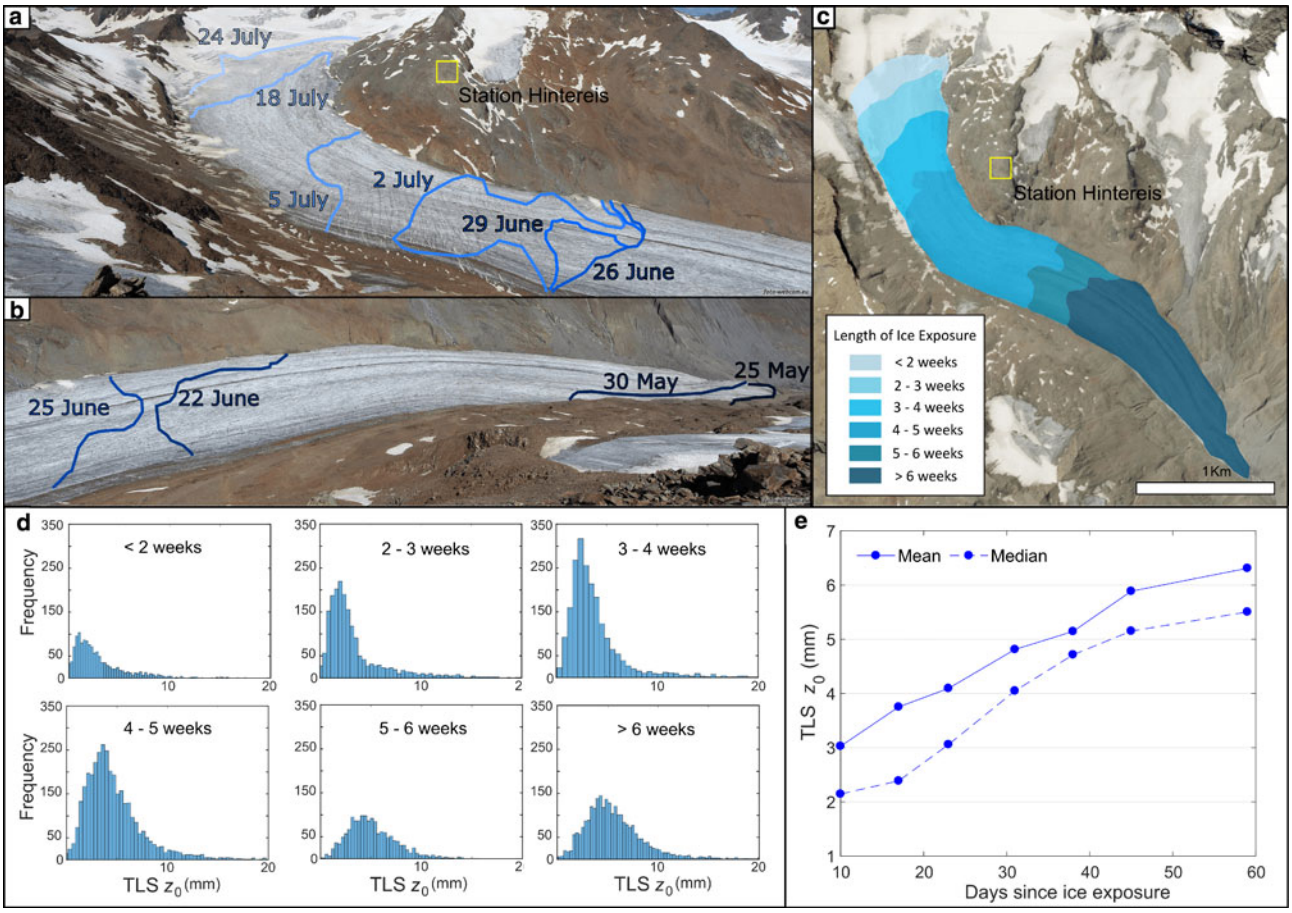

Fig. 9. (a) and (b) Digitised snow lines from time lapse cameras for upper and lower glacier, respectively. Imagery from www.foto-webcam.eu. (c) Polygons classifying glacier ice areas into zones of exposure length. (d) 3-D TLS z_0 estimates for each classified exposure zone. Estimates are made using the 3 August TLS survey. (e) Mean and median values of z_0 for areas of ice exposed to ablation for varying lengths of time.

debris-covered ice in the Himalaya, with $z_0 \gg 5$ mm, 3-D estimates of z_0 far exceeded 2-D estimates. Conversely, at Crevasse plots, 2-D z_0 estimates were larger than the 3-D estimates, as also observed by Smith and others (2016).

The difference in 2-D and 3-D z_0 estimates for different surface types most likely arises from the different way in which each method calculates frontal area. The 3-D method partially accounts for sheltering by ignoring all roughness elements below the detrended plane; the influence of this calculation step was most pronounced for Crevasse plots which contained extremely deep negative extensions below this plane. In contrast, the 2-D method included every point within a given transect and thus incorporated the effect of the deep crevasse as far as it was surveyed. As such, the 2-D method would generate the same value for an inverted crevasse transect as a regular crevasse. The approach of the 3-D method and its account for sheltering, therefore, seems reasonable given that a roughness element extending positively above the surface will likely impede the flow of air considerably more than a roughness element of the same size extending below the surface. Therefore, for plots with large roughness elements that extend above the detrended plane (e.g. Rock Pedestal and Dirt Cone) 3-D estimates exceed 2-D estimates and where roughness elements extended negatively below the detrended plane (e.g. Crevasses) 2-D estimates exceed 3-D estimates. Overall, the more sophisticated representation of sheltering possible and the increased availability of topographic data sufficient for 3-D z_0 estimates indicates that 3-D topographic methods will likely provide the source of z_0 values for use in distributed melt models.

Table 4. Mean change in 3-D z_0 over the period 3–16 August of classified exposure zones

Number of days exposed:	Change in 3-D z_0 (mm)
<2 weeks	1.46 [2.22]
2–3 weeks	1.40 [2.63]
3–4 weeks	0.74 [2.52]
4–5 weeks	0.56 [3.30]
5–6 weeks	0.42 [2.79]
>6 weeks	0.44 [3.31]

Standard deviation is in square brackets. See online Supplementary Table S2 for 2-D z_0 changes.

4.2 Plot-scale z_0 variability at Hintereisferner

The lowest values of z_0 recorded over Hintereisferner were between 1 and 5 mm for Smooth Ice, Dirty Ice and Compound surface types. These z_0 values are greater than some estimates of z_0, which for particularly smooth ice surfaces can be <1 mm (e.g. Grainger and Lister, 1966; Arnold and Rees, 2003; Giesen and others, 2009); yet, the values seem reasonable given that even the smoothest surfaces observed were visibly degraded and exhibited topographic variability. Indeed, the range of z_0 values observed over Hintereisferner compares more favourably with degraded and melting glacial ice surfaces in the literature (e.g. Greuell and Smeets, 2001; Sun and others, 2014; Guo and others, 2018). Pressure Ridge and Supraglacial Channel plots exhibited elongated roughness elements with z_0 ranging between 3 and 10 mm; estimates within the literature of z_0 over elongated glacier

ice hummocks range between 0.7 and 6.9 mm (e.g. Munro, 1989; Fitzpatrick and others, 2019), suggesting the values presented here are robust. Estimates of z_0 for Rock Pedestal and/or Dirt Cone plots have hitherto not been made; however, given the scale of roughness elements the larger estimates of z_0 of >10 mm predicted by 3-D methods seem reasonable. The most topographically variable surfaces over Hintereisferner were present at Crevasse plots, as reflected in high z_0 estimates for both 2-D and 3-D methods which are typically >20 mm. Smith and others (2016) recorded similarly large values over crevassed plots at Kårsaglaciären, while over very rough ice surfaces comparable values have been recorded (e.g. Obleitner, 2000; Smeets and van den Broeke, 2008; Azam and others, 2014).

Notably, our estimates of z_0 over Hintereisferner are typically larger than those obtained from similar studies utilising SfM imagery over bare ice surfaces (e.g. Irvine-Fynn and others, 2014; Smith and others, 2016). These higher z_0 values are likely a function of scale; the 10 m × 10 m plots utilised in this study are ~25× greater in area compared to the 2 m × 2 m plots utilised in these previous applications of the 2-D and 3-D z_0 estimation methods. Microtopographic estimations of z_0 have been found to show scale dependence, with z_0 increasing with plot size (Chambers and others, 2019). Therefore, when compared to the z_0 estimates of Irvine-Fynn and others (2014) and Smith and others (2016), higher values of z_0 for a similar surface should be expected. We assume herein that, despite this recognised scale dependence of z_0 values, their temporal evolution is relatively consistent within the length scale ranges of these plot-focused studies.

4.3 Upscaling z_0 estimates using TLS surveys

An assessment of the TLS z_0 estimates over a variety of different ice facies is presented in Figure 8. The map correctly identifies high and low values of z_0 for the steep ice exposures that contained crevasses and the smooth snow surfaces, respectively (d). Areas of the glacier with smooth ice surfaces and pressure ridges (f) are characterised by a z_0 ranging from ~2 to 7.5 mm throughout the upper glacier. Crevasses towards the edges of the glacier are particularly well highlighted (e) and are represented by z_0 values generally >12.5 mm and in some cases >50 mm. Relatively small, yet extreme, topographic features are also highlighted by high values of z_0 such as an area containing extensive debris cover, large rock pedestals (h), a large moulin (i) and the deep supraglacial channel network feeding it in the centre of the upper glacier. Due to a longer exposure of the ice surface, values of z_0 (ranging between 4 and 12.5 mm) over the lower glacier were typically greater than those over the upper glacier, characterising the topographic variability of the extensive network of supraglacial channels and hummocky ice present (g).

Surface roughness measured from the TLS surveys exhibited a stronger relationship with SfM estimated z_0 values than those achieved previously (e.g. Smith and others, 2016). This was potentially due to the larger plot size used over Hintereisferner, allowing for TLS scans to better reflect topographic variability when compared to the 2 m × 2 m plots studied by Smith and others (2016). The utility of TLS σ_d as a proxy for z_0 was further demonstrated by the finding that TLS σ_d values for separate ice facies fall into distributions similar to more detailed plot-scale z_0 estimates. The maps of z_0 estimates derived from TLS data facilitate clear visualisation of the variability of z_0 across Hintereisferner. Previous z_0 maps over bare ice surfaces have typically represented spatial variability by extrapolating point data (e.g. Brock and others, 2006). The maps presented here offer a step forward and could be readily applied in distributed melt SEB models. It should be noted, however, that model performance was weaker over Crevasse plots, especially for 2-D estimates, though this is perhaps related to the sheltering and SfM model quality issues mentioned above. Certainly, the approach demonstrated herein provides a more robust representation of z_0 than a constant value, as adopted by some SEB models (e.g. van As, 2011; Fausto and others, 2016*b*).

4.4 A scale-dependent model of the temporal variability of z_0

Several studies have reported considerable variation in z_0 over the course of an ablation season (e.g. Guo and others, 2011; Sicart and others, 2014; Fitzpatrick and others, 2019). Much of this variability is accounted for by differences in both wind speed and direction; however, the development of surface microtopography through time also has a significant effect. The effect of evolving topography on z_0 is to date relatively poorly understood and the literature shows multiple contrasting trends in the evolution of z_0 through time (e.g. Smeets and others, 1999; Smeets and van den Broeke, 2008; Smith and others, 2016). In an effort to unify these different perspectives, we adapted the three-stage model of Guo and others (2011) to propose a new scale-dependent theoretical model for predicting the evolution of z_0 throughout an ablation season.

Our model separates the temporal z_0 evolution model of Guo and others (2011) into five stages (Fig. 10a). Stage 1 details the transition of the surface from fresh snow cover, to a mixed snow and ice surface, at which z_0 reaches its first peak (as per Guo and others, 2011). Stage 2 maps the transition of the surface from this mixed cover to a bare ice surface and can take several trajectories depending on the roughness of the underlying ice surface (the suggested range of which is noted as grey dashed lines in Fig. 10a). Guo and others (2011) observed a decreasing z_0 as a flat ice surface was gradually exposed; conversely Smeets and van den Brooke (2008) noted an increase in z_0 at this stage at the Greenland ice sheet as ice hummocks were exposed. No observations were made of these two stages at Hintereisferner; however, the relatively rough underlying ice observed in the field indicates that a substantial decrease in z_0 during stage 2 is unlikely. Our field observations begin at stage 3 which represents a period of time between ice exposure and the clear development of surface features, during which only small channels are present in the surface and ice hummocks are yet to develop. In stage 4 z_0 rapidly increases, as surface features are established and are pronounced by increasing melt rates and the development of a complex meltwater channel network. During stage 5, z_0 approaches its peak value beyond which the density of some smaller-scale roughness elements will reach values where wake-interference and skimming flow are initiated thereby decreasing z_0.

To inform the development of the theoretical model, each plot (excluding Rock Pedestal and Crevasse plots) was placed on the proposed model and a simplification of the z_0 trajectory indicated (Fig. 10b). Following the space-for-time substitution in Figure 9, plots located towards the lower end of the glacier, over which the ice surface had been exposed for a longer time period, appear further along the transition model. Field observations of the ice surface were used to guide the overall positioning along the theoretical curve. The trajectory of z_0 values within the plots rarely followed the anticipated trajectory. Indeed, the theoretical model predicts an increasing value of z_0; contrastingly, plot-scale z_0 estimates showed highly variable trajectories with an overall decrease in z_0 for the majority of plots, despite the existence of pronounced surface features. Two of the Smooth Ice (P8 and P9) plots, which would be expected to be characterised by a relatively constant z_0, demonstrated a variable value of z_0 which decreased over the course of observation. Overall, only three

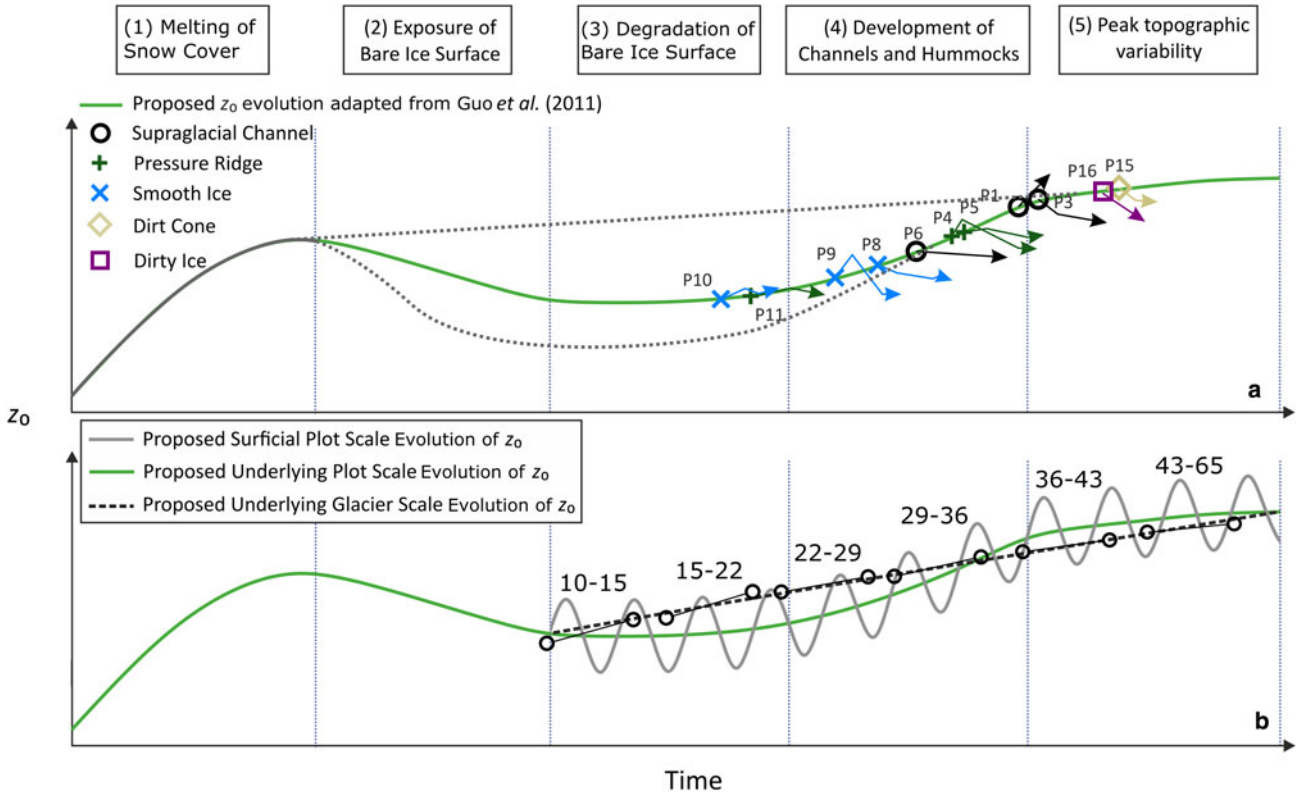

Fig. 10. (a) Initial, five-stage theoretical model for z_0 development during the ablation season (developed from Guo and others (2011) where stages 2–4 were grouped together). Temporal evolution of the ice facies observed over Hintereisferner is also indicated (excluding Compound, Rock Pedestal and Crevasse plots). (b) Proposed scale-dependent theoretical models with indications of where observed changes to each exposure zone over study duration would fall on model, based on field observation.

plots (P10, P11 and P1) exhibited the expected evolution of z_0 anticipated from the model.

Here we argue that scale plays an important role in determining how the temporal evolution of z_0 is observed. At the plot scale, the complex interaction of preferential melt and meltwater channel development controls the microtopography of the surface at Hintereisferner. The simple model proposed in Figure 10a is certainly inadequate and cannot represent the variability of z_0 due to these processes. The variability in the trajectory of z_0 is high and is unlikely to reveal any underlying progressive evolution of z_0 ice surfaces except over long time periods. Plot-scale trajectories of z_0 appear to be relatively unpredictable and independent of the ice facies, contrasting the findings of Smith and others (2016). Other studies suggest that the diversity of plot-scale z_0 trajectories is most pronounced following the initial melt of the snow surface. At the plot scale, Fitzpatrick and others (2019) measured z_0 over the course of an entire ablation season using sonic anemometers and observed an initial rise in z_0 as snow cover melts to form sun cups, supporting the underlying plot-scale evolution of z_0. Following the initial rise, they recorded a period of 60 d with no trend in z_0, potentially reflecting the relatively stable behaviour of z_0 through late stage 2 to early stage 4. Similarly, Brock and others (2006) recorded wind profile and microtopographic estimations of z_0 across the course of the 1993 and 1994 ablation seasons of Haut Glacier D'Arolla, Switzerland. Although their z_0 observations over snow surfaces support the progression proposed in stage 1, they observed a number of different temporal trends in the evolution of z_0 values over exposed ice surfaces, including a declining value of z_0 towards the end of the ablation season.

The underlying progression of z_0 can only be revealed through observations of greater spatial scales, over which the unpredictable behaviour of individual plot values are aggregated into a more predictable trajectory. Figure 10b presents a visual representation of this theoretical z_0 evolution model. At the glacier scale, TLS derived z_0 estimates display a constant and relatively linear increase in mean z_0 at a rate of ~0.10 mm d^{-1}, over the 15 d observation period (Fig. 10b). The space-for-time substitution of Figure 9 lends further support to the notion of a progressive increase in z_0 over a 50 d period, with a slightly slower increase in the mean z_0 of ~0.07 mm d^{-1}. Observed changes in z_0 within exposure zones (Table 4) indicate a more-or-less linear increase during the study period. While older exposed surfaces experience smaller increases than more recently exposed surfaces, the reduction in gradient is not as pronounced as suggested in the underlying theoretical model. This theoretical glacier-scale behaviour is supported by the spatially distributed maps of z_0 presented in Brock and others (2006), who over six periods throughout the melt season, observed a clear increase in glacier-scale z_0 with the onset of melt, continuing until snowfall at the end of the ablation season, at which point a lowering of z_0 is observed at a number of sites.

4.5 Further work

Both 2-D and 3-D z_0 estimates have been demonstrated to reasonably approximate aerodynamically derived z_0 values (Quincey and others, 2017; Chambers and others, 2019); yet, further consideration of the drag coefficient (Quincey and others, 2017), the influence of sheltering effects and scale dependencies of microtopographically derived z_0 would give estimates a stronger theoretical foundation.

The proposed scale-dependent trajectories of z_0 outlined in Figure 10 infers the behaviour of z_0 over an entire ablation season. Yet, plot-based estimates of z_0 observed at Hintereisferner had a maximum measurement period of 14 d, with some plots being observed over shorter time periods and glacier-scale TLS-based

estimates spanning 13 d only. Although the time period was extended to ~50 d using a space-for-time substitution, the results of which supported a progressive increase in z_0, the conclusions presented herein are limited by the short duration over which observations were made. The space-for-time substitution should be treated with some caution, given the potential for longitudinal glacier interactions, notably the downstream transfer of meltwater, which may influence the signal observed. Certainly, a longer observation period would allow for a clearer assessment of the accuracy of the theoretical model proposed.

Finally, with a larger number of plot-scale observations, a more objective classification of ice surface facies becomes possible, potentially based on observed roughness metrics from glacier-scale surveys. Such distributed maps of ice surface type could then better inform the production of distributed z_0 maps via individual regression relationships for each surface type. The incorporation of such z_0 maps into a distributed SEB model represents the key focus for further research, though there remains the question of how much detail of z_0 variability in both space and time is required to have a substantial impact on turbulent flux estimation.

5. Conclusions

This research adds to a growing literature (e.g. Brock and others, 2006; Smeets and van den Broeke and others, 2008; Guo and others, 2011; Smith and others, 2016; Quincey and others, 2017; Fitzpatrick and others, 2019) that emphasises the need to more comprehensively represent z_0 in SEB models to reduce errors in estimates of ablation. Specifically, the assumption of a constant z_0 value over ice surfaces, commonly 1 mm (e.g. van As, 2011), requires improvement. Representing z_0 more accurately in SEB models is especially important given the increasing contribution of turbulent fluxes to glacier SEB as the climate becomes wetter, windier and warmer.

The recent proliferation of high-resolution topographic data acquisition techniques has advanced the potential for estimations of z_0 and enabled effective relationships to be developed to upscale plot results to the glacier scale. The use of 3-D methods to estimate z_0 makes the best use of this available data. Plot scale estimates of z_0 demonstrated substantial variability in both space and time, ranging from $z_0 < 3$ mm to $z_0 > 40$ mm. z_0 over such surfaces can change at rates in excess of 0.25 mm d^{-1} as the surface melts and can be due to complex interactions between meltwater channel development and preferential melt. At the glacier scale, spatial variability in z_0 values was >2 orders of magnitude but a consistent increase in z_0 of 0.07–0.10 mm d^{-1} was observed.

Our findings indicate that glacier scale topographic datasets can usefully capture the variability in ice surface roughness that is relevant for the estimation of z_0. While a TLS was available for this study, airborne laser scanning or even satellite-derived datasets that are more widely available may provide sufficient topographic information to estimate z_0 variability in space and time to the extent that is required by distributed melt models.

Overall, we contend that by interpreting the temporal trends in z_0 as a function of the spatial scale over which they are observed, our theoretical z_0 model goes some way towards unifying a variety of contrasting temporal trends observed within the wider literature. The interpretation presented here is that plot scale trends in z_0 are stochastic in the short term but by extending either the length of observation or the spatial scale underlying trends in z_0 are revealed. Further work into theoretical scale-dependent behaviour of z_0 through time is required. If such work supports a progressive increase in z_0, constraining the rate of this increase may pave the way for representation of the temporal development of z_0 in SEB models.

Supplementary material. The supplementary material for this article can be found at https://doi.org/10.1017/jog.2020.56

Acknowledgements. Fieldwork was funded by an INTERACT transnational access grant awarded to MWS under the European Union H2020 Grant Agreement No. 730938. The TLS facility is financed by the University of Innsbruck and jointly operated by the Department of Geography and the Department of Atmospheric and Cryospheric Research. JRC is supported by a NERC PhD studentship (NE/L002574/1). IS was funded by Austrian Science Fund (FWF) grant T781-N32. The authors acknowledge Matt Westoby and Andy Baird and two anonymous reviewers for constructive comments on this work. The authors declare that they have no conflicts of interest.

References

Ambach W (1961) Die Bedeutung des aufgefrorenen Eises für den Massen- und Energiehaushalt der Gletscher. *Zeitschrift für Gletscherkunde und Glazialgeologie* **4**, 169–189.

Anslow FS, Hostetler S, Bidlake WR and Clark PU (2008) Distributed energy balance modeling of South Cascade Glacier, Washington and assessment of model uncertainty. *Journal of Geophysical Research: Earth Surface* **113**(F2), F02019. doi:10.1029/2007JF000850.

Arnold NS and Rees WG (2003) Self-similarity in glacier surface characteristics. *Journal of Glaciology* **49**(167), 547–554. doi:10.3189/172756503781830368.

Azam MF and 6 others (2014) Processes governing the mass balance of Chhota Shigri Glacier (western Himalaya, India) assessed by point-scale surface energy balance measurements. *The Cryosphere* **8**(6), 2195–2217. doi:10.5194/tc-8-2195-2014.

Behrens H, Bergmann H, Moser H, Ambach W and Jochum O (1975) On the water channels of the internal drainage system of the Hintereisferner, Ötztal Alps, Austria. *Journal of Glaciology* **14**(72), 375–382. doi:10.3189/S0022143000021900.

Belart JMC and 9 others (2017) Winter mass balance of Drangajökull ice cap (NW Iceland) derived from satellite sub-meter stereo images. *The Cryosphere* **11**, 1501–1517.

Bintanja R and van den Broeke MR (1995) Momentum and scalar transfer coefficients over aerodynamically smooth Antarctic surfaces. *Boundary-Layer Meteorology* **74**(1-2), 89–111. doi:10.1007/BF00715712.

Blümcke A and Hess H (1899) Untersuchungen am Hintereisferner. *Wissenschaftliche Ergänzungshefte zur Zeitschrift des Deutschen und Österreichischen Alpenvereins* **1**(2), 1–87.

Brasington J, Vericat D and Rychkov I (2012) Modeling river bed morphology, roughness, and surface sedimentology using high resolution terrestrial laser scanning. *Water Resources Research* **48**, W11519. doi: doi:10.1029/2012WR012223.

Bravo C, Loriaux T, Rivera A and Brock B (2017) Assessing glacier melt contribution to streamflow at Universidad Glacier, central Andes of Chile. *Hydrology and Earth System Sciences* **21**(7), 3249–3266. doi:10.5194/hess-21-3249-2017.

Brock BW, Willis IC and Sharp MJ (2006) Measurement and parameterization of aerodynamic roughness length variations at Haut Glacier d'Arolla, Switzerland. *Journal of Glaciology* **52**(177), 281–297. doi:10.3189/172756506781828746.

Brock BW, Willis IC, Sharp MJ and Arnold NS (2000) Modelling seasonal and spatial variations in the surface energy balance of Haut Glacier d'Arolla, Switzerland. *Annals of Glaciology* **31**, 53–62. doi:10.3189/172756400781820183.

Carrivick JL and 7 others (2015*a*) Decadal-scale changes of the Ödenwinkelkees, central Austria, suggest increasing control of topography and evolution towards steady state. *Geografiska Annaler: Series A, Physical Geography* **97**(3), 543–562. doi:10.1111/geoa.12100.

Carrivick JL, Smith MW and Carrivick DM (2015*b*) Terrestrial laser scanning to deliver high-resolution topography of the upper Tarfala valley, arctic Sweden. *GFF* **137**(4), 383–396. doi:10.1080/11035897.2015.1037569.

Chambers J and 5 others (2019) Glacial aerodynamic roughness estimates: uncertainty, sensitivity and precision in field measurements. *Journal of Geophysical Research: Earth Surface* **125**(2). doi:10.1029/2019JF005167.

Conway JP and Cullen NJ (2016) Cloud effects on surface energy and mass balance in the ablation area of Brewster Glacier, New Zealand. *The Cryosphere* **10**(1), 313–328. doi:10.5194/tc-10-313-2016,, 2016.

Cuffey KM and Paterson WSB (2010) *The Physics of Glaciers*, 4th ed. Oxford: Butterworth-Heinemann.

Deschamps-Berger C and 7 others (2020) Snow depth mapping from stereo satellite imagery in mountainous terrain: evaluation using airborne lidar data. *The Cryosphere Discussions* doi:10.5194/tc-2020-15.

Ebrahimi S and Marshall SJ (2016) Surface energy balance sensitivity to meteorological variability on Haig Glacier. *Canadian Rocky Mountains. The Cryosphere* **10**(6), 2799–2819. doi:10.5194/tc-10-2799-2016.

Escher-Vetter H, Kuhn M and Weber M (2009) Four decades of winter mass balance of Vernagtferner and Hintereisferner, Austria: methodology and results. *Annals of Glaciology* **50**(50), 87–95. doi:10.3189/172756409787769672.

Fausto RS and 5 others (2016*a*) The implication of nonradiative energy fluxes dominating Greenland ice sheet exceptional ablation area surface melt in 2012. *Geophysical Research Letters* **43**(6), 2649–2658. doi:10.1002/2016GL067720.

Fausto RS, van As D, Box JE, Colgan W and Langen PL (2016*b*) Quantifying the surface energy fluxes in south Greenland during the 2012 high melt episodes using in-situ observations. *Frontiers in Earth Science* **4**, 82. doi:10.3389/feart.2016.00082.

Favier V and 5 others (2011) Modelling the mass and surface heat budgets in a coastal blue ice area of Adelie Land, Antarctica. *Journal of Geophysical Research: Earth Surface* **116**(F3), F03017. doi:10.1029/2010JF001939.

Fischer A (2010) Glaciers and climate change: interpretation of 50 years of direct mass balance of Hintereisferner. *Global and Planetary Change* **71**(1–2), 13–26. doi:10.1016/j.gloplacha.2009.11.014.

Fischer A, Seiser B, Stocker Waldhuber M, Mitterer C and Abermann J (2015) Tracing glacier changes in Austria from the Little Ice Age to the present using a lidar-based high-resolution glacier inventory in Austria. *The Cryosphere* **9**(2), 753–766. doi:10.5194/tc-9-753-2015.

Fitzpatrick N, Radić V and Menounos B (2019) A multi-season investigation of glacier surface roughness lengths through in situ and remote observation. *The Cryosphere* **13**(3), 1051–1071. doi:10.5194/tc-13-1051-2019.

Franco B, Fettweis X and Erpicum M (2013) Future projections of the Greenland ice sheet energy balance driving the surface melt. *The Cryosphere* **7**(1), 1–18. doi:10.5194/tc-7-1-2013.

Geist T and Stotter J (2007) Documentation of glacier surface elevation change with multi-temporal airborne laser scanner data--case study: Hintereisferner and Kesselwandferner, Tyrol, Austria. *Zeitschrift fur Gletscherkunde und Glazialgeologie* **41**, 77–106.

Giesen RH, Andreassen LM, Oerlemans J and van den Broeke MR (2014) Surface energy balance in the ablation zone of Langfjordjøkelen, an arctic, maritime glacier in northern Norway. *Journal of Glaciology* **60**(219), 57–70. doi:10.3189/2014JoG13J063.

Giesen RH, Andreassen LM, van den Broeke MR and Oerlemans J (2009) Comparison of the meteorology and surface energy balance at Storbreen and Midtdalsbreen, two glaciers in southern Norway. *The Cryosphere* **3**, 57–74. doi:10.5194/tc-3-57-2009.

Grainger ME and Lister H (1966) Wind speed, stability and eddy viscosity over melting ice surfaces. *Journal of Glaciology* **6**(43), 101–127. doi:10.3189/S0022143000019109.

Greuell W (1992) Hintereisferner, Austria: mass-balance reconstruction and numerical modelling of the historical length variations. *Journal of Glaciology* **38**(129), 233–244. doi:10.3189/S0022143000003646.

Greuell W and Genthon C (2004) Modelling land-ice surface mass balance. In Bamber JL and Payne AJ (eds), *Mass Balance of the Cryosphere: Observations and Modelling of Contemporary and Future Changes*. Cambridge: Cambridge University Press, pp. 117–168. doi:10.1017/S0016756805251701.

Greuell W and Smeets P (2001) Variations with elevation in the surface energy balance on the Pasterze (Austria). *Journal of Geophysical Research: Atmospheres* **106**(D23), 31717–31727. doi:10.1029/2001JD900127.

Gromke C, Manes C, Walter B, Lehning M and Guala M (2011) Aerodynamic roughness length of fresh snow. *Boundary-Layer Meteorology* **141**(1), 21–34. doi:10.1007/s10546-011-9623-3.

Guo X and 7 others (2011) Critical evaluation of scalar roughness length parametrizations over a melting valley glacier. *Boundary-layer Meteorology* **139**(2), 307–332. doi:10.1007/s10546-010-9586-9.

Guo S and 10 others (2018) Simple parameterization of aerodynamic Roughness lengths and the turbulent heat fluxes at the Top of midlatitude August-One Glacier, Qilian Mountains, China. *Journal of Geophysical Research: Atmospheres* **123**(21), 12–66. doi:10.1029/2018JD028875.

Hock R and Holmgren B (2005) A distributed surface energy-balance model for complex topography and its application to Storglaciären, Sweden. *Journal of Glaciology* **51**(172), 25–36. doi:10.3189/172756505781829566.

Hoffman MJ, Fountain AG and Liston GE (2008) Surface energy balance and melt thresholds over 11 years at Taylor Glacier, Antarctica. *Journal of Geophysical Research: Earth Surface* **113**(F4), F04014. doi:10.1029/2008JF001029.

Irvine-Fynn T, Sanz-Ablanedo E, Rutter N, Smith M and Chandler J (2014) Measuring glacier surface roughness using plot-scale, close-range digital photogrammetry. *Journal of Glaciology* **60**(223), 957–969. doi:10.3189/2014JoG14J032.

Ishikawa N, Owens IF and Sturman AP (1992) Heat balance characteristics during fine periods on the lower parts of the Franz Josef Glacier, South Westland, New Zealand. *International Journal of Climatology* **12**(4), 397–410. doi:10.1002/joc.3370120407.

James MR, Robson S, d'Oleire-Oltmanns S and Niethammer U (2017*b*) Optimising UAV topographic surveys processed with structure-from-motion: ground control quality, quantity and bundle adjustment. *Geomorphology* **280**, 51–66. doi:10.1016/j.geomorph.2016.11.021.

Klug C and 8 others (2018) Geodetic reanalysis of annual glaciological mass balances (2001–2011) of Hintereisferner, Austria. *The Cryosphere* **12**(3), 833–849. doi:10.5194/tc-12-833-2018.

Koelemeijer R, Oerlemans J and Tjemkes S (1993) Surface reflectance of Hintereisferner, Austria, from Landsat 5 TM imagery. *Annals of Glaciology* **17**, 17–22. doi:10.3189/S0260305500012556

Kuhn M and 5 others (1999) Measurements and models of the mass balance of Hintereisferner. *Geografiska Annaler: Series A. Physical Geography* **81**(4), 659–670. doi:10.1111/1468-0459.00094.

Kutzbach JE (1961) *Investigations of the modification of wind profiles by artificially controlled surface roughness*. (Ph.D. thesis, University of Wisconsin)

Lambrecht A and Kuhn M (2007) Glacier changes in the Austrian Alps during the last three decades, derived from the new Austrian glacier inventory. *Annals of Glaciology* **46**, 177–184. doi:10.3189/172756407782871341.

Lettau H (1969) Note on aerodynamic roughness-parameter estimation on the basis of roughness-element description. *Journal of Applied Meteorology* **8** (5), 828–832. doi:10.1175/1520-0450(1969)008<0828:NOARPE>2.0.CO;2.

Lewis KJ, Fountain AG and Dana GL (1998) Surface energy balance and meltwater production for a Dry Valley glacier, Taylor Valley, Antarctica. *Annals of Glaciology* **27**, 603–609. doi:10.3189/1998AoG27-1-603-609.

Marti R and 5 others (2016) Mapping snow depth in open alpine terrain from stereo satellite imagery. *The Cryosphere* **10**, 1361–1380.

Miles ES, Steiner JF and Brun F (2017) Highly variable aerodynamic roughness length (*z*0) for a hummocky debris-covered glacier. *Journal of Geophysical Research: Atmospheres* **122**(16), 8447–8466. doi:10.1002/2017JD026510

Morris EM (1989) Turbulent transfer over snow and ice. *Journal of Hydrology* **105**(3–4), 205–223. doi:10.1016/0022-1694(89)90105-4.

Munro DS (1989) Surface roughness and bulk heat transfer on a glacier: comparison with eddy correlation. *Journal of Glaciology* **35**(121), 343–348. doi:10.3189/S0022143000009266

Nicholson LI, Petlicki M, Partan B and MacDonell S (2016) 3D Surface properties of glacier penitentes over an ablation season, measured using a Microsoft Xbox Kinect. *Cryosphere* **10**(5), 1897–1913. doi:10.5194/tc-10-1897-2016.

Obleitner F (1994) Climatological features of glacier and valley winds at the Hintereisferner (Ötztal Alps. Austria). *Theoretical and Applied Climatology* **49**(4), 225–239. doi:10.1007/BF00867462.

Obleitner F (2000) The energy budget of snow and ice at Breidamerkurjökull, Vatnajökull, Iceland. *Boundary-layer Meteorology* **97**(3), 385–410. doi:10.1023/A:1002734303353.

O'Connor J, Smith MJ and James MR (2017) Cameras and settings for aerial surveys in the geosciences: optimising image data. *Progress in Physical Geography* **41**(3), 325–344. doi:10.1177/0309133317703092.

Patzelt G (1970) Die Längenmessungen an den Gletschern der österreichischen Ostalpen 1890–1969. *Zeitschrift für Gletscherkunde und Glazialgeologie* **6**(1–2), 151–159.

Patzelt G (1980) The Austrian glacier inventory: status and first results. *International Association of Hydrological Sciences* **126**, 181–183.

Quincey D and 5 others (2017) Evaluating morphological estimates of the aerodynamic roughness of debris covered glacier ice. *Earth Surface Processes and Landforms* **42**(15), 2541–2553. doi:10.1002/esp.4198.

Radić V and 5 others (2017) Evaluation of different methods to model near-surface turbulent fluxes for a mountain glacier in the Cariboo Mountains, BC, Canada. *The Cryosphere* **11**(6), 2897–2918. doi:10.5194/tc-11-2897-2017.

Rees WG and Arnold NS (2006) Scale-dependent roughness of a glacier surface: implications for radar backscatter and aerodynamic roughness modelling. *Journal of Glaciology* **52**(177), 214–222. doi:10.3189/172756506781828665.

RIEGL (2019) *Data Sheet RIEGL VZ*-6000. [Online]. [Accessed 23 July 2019]. Available from: http://www.riegl.com/uploads/tx_pxpriegldownloads/RIEGL_VZ-6000_Datasheet_2019-05-28_01.pdf.

Schmidt LS and 7 others (2017) The importance of accurate glacier albedo for estimates of surface mass balance on Vatnajökull: evaluating the surface energy budget in a regional climate model with automatic weather station observations. *The Cryosphere* **11**(4), 1665–1684. doi:10.5194/tc-11-1665-2017.

Shaw TB, Gascoin S, Mendoza PA, Pellicciotti F and McPhee J (2020) Snow depth patterns in a high mountain Andean catchment from satellite optical tristereoscopic remote sensing. *Water Resources Research* **56**, e2019W, R024880.

Shean DE and 5 others (2020) A systematic, regional assessment of high mountain Asia Glacier mass balance. *Frontiers in Earth Science* **7**, 363.

Sicart JE, Litt M, Helgason W, Tahar VB and Chaperon T (2014) A study of the atmospheric surface layer and roughness lengths on the high-altitude tropical Zongo glacier, Bolivia. *Journal of Geophysical Research: Atmospheres* **119**(7), 3793–3808. doi:10.1002/2013JD020615.

Sicart JE, Wagnon P and Ribstein P (2005) Atmospheric controls of the heat balance of Zongo Glacier (16 S, Bolivia). *Journal of Geophysical Research: Atmospheres* **110**(D12), D12106. doi:10.1029/2004JD005732.

Smeets CJPP, Duynkerke PG and Vugts HF (1999) Observed wind profiles and turbulence fluxes over an ice surface with changing surface roughness. *Boundary-Layer Meteorology* **92**(1), 99–121. doi:10.1023/A:1001899015849.

Smeets CJPP and van den Broeke MR (2008) Temporal and spatial variations of the aerodynamic roughness length in the ablation zone of the Greenland ice sheet. *Boundary-Layer Meteorology* **128**(3), 315–338. doi:10.1007/s10546-008-9291-0.

Smith MW (2014) Roughness in the earth sciences. *Earth-Science Reviews* **136**, 202–225. doi:10.1016/j.earscirev.2014.05.016.

Smith MW and 6 others (2016) Aerodynamic roughness of glacial ice surfaces derived from high-resolution topographic data. *Journal of Geophysical Research: Earth Surface* **121**(4), 748–766. doi:10.1002/2015JF003759.

IPCC (2013) Information from paleoclimate archives. In Stocker TF, Qin D, Plattner GK, Tignor M, Allen SK, Boschung J, Nauels A, Xia Y, Bex V and Midgley PM (eds), *Climate Change 2013: The Physical Science Basis. Contribution of Working Group I to the Fifth Assessment Report of the Intergovernmental Panel on Climate Change*. Cambridge, United Kingdom and New York, NY, USA: Cambridge University Press, pp. 383–464. doi:10.1017/CBO9781107415324.

Strasser U and 10 others (2018) The Rofental: a high Alpine research basin (1890–3770 m asl) in the Ötztal Alps (Austria) with over 150 years of hydrometeorological and glaciological observations. *Earth System Science Data* **10**(1), 151. doi:10.5194/essd-10-151-2018.

Sun W and 9 others (2014) Ablation modeling and surface energy budget in the ablation zone of Laohugou glacier No. 12, western Qilian mountains, China. *Annals of Glaciology* **55**(66), 111–120. doi:10.3189/2014AoG66A902.

Sun W and 6 others (2018) The response of surface mass and energy balance of a continental glacier to climate variability, western Qilian Mountains, China. *Climate Dynamics*. **50**(9–10), 3557–3570. doi:10.1007/s00382-017-3823-6.

van As D (2011) Warming, glacier melt and surface energy budget from weather station observations in the Melville Bay region of northwest Greenland. *Journal of Glaciology* **57**(202), 208–220. doi:10.3189/002214311796405898.

van den Broeke MR and 5 others (2008) Partitioning of melt energy and meltwater fluxes in the ablation zone of the west Greenland ice sheet. *The Cryosphere* **2**(2), 179. doi:10.5194/tc-2-179-2008.

van den Broeke MR, Smeets CJPP and van de Wal RSW (2011) The seasonal cycle and interannual variability of surface energy balance and melt in the ablation zone of the west Greenland ice sheet. *The Cryosphere* **5**(2), 377–390. doi:10.5194/tc-5-377-2011.

van de Wal RSW, Oerlemans J and van der Hage JC (1992) A study of ablation variations on the tongue of Hintereisferner, Austrian Alps. *Journal of Glaciology* **38**(130), 319–324. doi:10.3189/S0022143000002203.

Vincent C and 9 others (2017) Common climatic signal from glaciers in the European Alps over the last 50 years. *Geophysical Research Letters* **44**(3), 1376–1383. doi:10.1002/2016GL072094.